Transient interactions drive the lateral clustering of Cadherin-23 on membrane

Cheerneni S Srinivas[1#], Gayathri S Singaraju[1#], Veerpal Kaur[1], Sayan Das[1], Sanat K. Ghosh[2], Amin Sagar[1], Anuj Kumar[2,3], Tripta Bhatia[2*], and Sabyasachi Rakshit[1,3*]

[1]Department of Chemical Sciences, Indian Institute of Science Education and Research Mohali, Punjab, India.

[2]Department of Physical Sciences, Indian Institute of Science Education and Research Mohali, Punjab, India.

[3]Centre for Protein Science Design and Engineering, Indian Institute of Science Education and Research Mohali, Punjab, India.

[*]Correspondence to Sabyasachi Rakshit

Email: srakshit@iisermohali.ac.in

triptabhatia@iisermohali.ac.in

[#] Equal contributions

Abstract

Cis and trans-interactions in cadherins are the foundations of multicellularity. While the molecular structure of trans-interactions of cadherins is well understood, the molecular cues in cis-interactions are still unidentified for many cadherins. Further, the molecular mechanisms that steer the linear array of cis-clustering to a two-dimensional cell-cell junction are still dubious. Here we report that weak and transient intermolecular interactions requisite for liquid-liquid phase separations of biomolecules in solution, may drive the cis-clustering of cadherins on a membrane. We noted that cadherin-23, a non-classical cadherin with an extended extracellular region, does not engage in cis-dimerization. However, it forms spherical liquid droplets in solution and two-dimensional cis-clusters on a membrane without any trans-mediated anchorage. In cellulo, the cis-clustering accelerates the cell-cell adhesion and, thus, kinetically controls cell-adhesion via the cis-precedes-trans model. Though the physiological connection of cis-clustering with the rapid adhesion is yet to explore, M2-macrophages that predominantly express cadherin-23 undergo fast attachments to circulatory tumor cells during metastasis.

Introduction

Cadherins predominantly maneuver the active cell-adhesion processes for both vertebrates and invertebrates. Two modes of binding are known for cadherins, trans-binding and cis-binding. While in trans-binding, the terminal extracellular (EC) domains of cadherins from opponent cells interact, the cis-binding is mediated by the lateral interactions among the rest of the EC domains

of cadherins from the same cell surfaces(Harrison et al., 2011). For classical cadherins, the trans mediates direct contacts among opposing cells via a diffusion-trap kinetic approach and secures a cell-cell junction. Approximately a cluster of five independent classical E(pithelial)-cadherin proteins diffuse across the membrane and form the trans-mediated cell-cell adherin junctions with neighboring cells (Wu et al., 2015). Lateral or cis-interactions, thereafter, influence the clustering of cadherins on the premature junctions and strengthen the association between cells. Two specific cis-interactions are identified in the crystal lattice of N-, C-, or E-cadherins that extend the intercellular junction linearly. The molecular pathway that laid the transition from a linear array to the two-dimensional cadherin junctions on the cell surface is still unidentified. For type I cadherins, it is proposed that a combination of cis and trans-interactions via exclusive shape complementarity form the two-dimensional adherens surface. We propose that nonspecific and transient intermolecular interactions may drive a two-dimensional arrangement of cadherins on cell membranes without any trans-mediated anchorage to the cell-cell junction.

Clustering of solute in a solution is a typical example of phase separation. In cell biology, such a liquid-liquid phase separation (LLPS) is common in the cytoplasm. It is the developmental origin of the membrane-less liquid compartments like nucleoli(Latonen, 2019), centrosomes(Mahen and Venkitaraman, 2012), Cajal bodies(Gall, 2003), stress granules(Buchan and Parker, 2009). Relatively uncommon, but the existence of LLPS is also reported with proteins like Zonula Occludens (Beutel et al., 2019) and nephrin(Banjade and Rosen, 2014) that are anchored to cell-membrane and mediate multiprotein cell-adhesion, signal transduction. Transient, weak, and favorable nonspecific interactions among like-neighbors are thermodynamically responsible for such phase separations. Such favorable interactions may drive cis-clustering of cadherins on two-dimensional confinement; without any trans- or stable cis-dimeric interactions.

We performed an unbiased *in silico* search using the catGRANULE algorithm (Mitchell et al., 2013, Klus et al., 2014) across the cadherin-superfamily of proteins and identified cadherin-23 (Cdh23) (NP_075859) protein with a high propensity to undergo LLPS. Cdh23 is one of the long non-classical classes of cadherins with 27 extracellular domains. The two outermost domains of Cdh23 from opposing cells interact homophilically in a trans-conformation and mediate strong cell-cell adhesion among tissues like the heart, kidney, muscle, and testis (Sannigrahi et al., 2019, Singaraju et al., 2019, Sotomayor et al., 2012). The two-outermost domains of Cdh23 also interact heterophilically with protocadherin-15 in the neuroepithelial cells of the inner ear and serve as gating-springs for mechanotransduction in hearing (Sotomayor et al., 2010). Apart from the trans-complexes, no other stable or metastable dimers of Cdh23 were detected in the solution from the photoinduced cross-linking of unmodified proteins (PICUP). However, we noticed a spontaneous formation of liquid droplets of Cdh23 in solution upon the tuning of the counterbalancing interactions among extracellular domains of Cdh23 with ions and spacers and lateral clustering on individual vesicle membranes. Notably, the two terminal domains that form trans-interactions, either homophilic or heterophilic, were neutralized during clustering on membrane or phase separation in solution. It is well-known that chemical needles like 1,6-Hexanediol (HD) rupture liquid droplets of biomacromolecules by non-specifically blocking intermolecular interactions (Patel et al., 2017). We noticed no LLPS of Cdh23 *in-vitro* after 1,6-

HD treatment. The lateral clustering of cadherins on the vesicle membrane was also ruptured by 1,6-HD.

Free-standing cis-clustering of Cdh23 independent of trans-binding prompted us to study the effect of clustering on cell adhesion. We measured a significant acceleration in the rate of cell-cell adhesions driven by cis-clustering. Disruption of cis-clusters by 1,6-HD drastically dropped the rate, indicating the functional implication of cis-clustering in cell-cell adhesion. Notably, while the toxicity of the phase-separated states has already been proposed for intrinsically disordered proteins(Elbaum-Garfinkle, 2019), the fast-aggregation of cells is a demonstration of the functional implication of LLPS in cell adhesion.

Results

Cdh23 does not exist as cis-dimer in solution up to a concentration of 5 μM

Cdh23 is an extensively elongated protein with an EC region of ~315 kD. Traditional methods such as native gel electrophoresis and chromatography often fail to detect the higher-order complexes of Cdh23 if they exist. Here, we performed the photoinduced cross-linking of unmodified proteins (PICUP) to capture the stable or metastable dimers or oligomers of Cdh23 in the solution. PICUP is preferred for such identification due to its short reaction time, the ability to arrest short-lived assemblies, and, most importantly, no modification in the native proteins (Fancy and Kodadek, 1999). PICUP captures the short-lived dimer by forming radical-induced covalent bonds between two monomers. Followed by PICUP, we performed one-dimensional gel electrophoresis to obtain the stoichiometric distribution of dimer and monomer of proteins in equilibrium (Fig. 1 A). To increase the detection ability to ≥ 3 ng /protein, we used silver staining of PAGE. We noticed a dimer band for Cdh23 in PICUP. It is important to note that Cdh23 has a strong affinity to a trans-homodimer (Sannigrahi et al., 2019, Singaraju et al., 2019, Altin and Pagler, 1995). Upon blocking the trans-interactions using an excess of Cdh23 EC1-2 in solution, we detected no trace of Cdh23-dimer in the SDS-PAGE even at 5 μM of protein, indicating a poor affinity of Cdh23 towards cis-dimerization (Fig. 1 B). Cdh23 predominantly remains as a monomer even at a high concentration of 5 μM.

Cdh23 with 27 EC domains undergoes LLPS

Though Cdh23 does not form cis-dimers in solution, we observed a spontaneous phase separation (LLPS) of Cdh23 in the liquid phase from solution upon increasing entropy in the system. The fundamental difference in the nature of interactions in higher-order complexation and phase separation is the interaction strength and specificity. While protein-protein complex formation relies on relatively stable and specific interactomes, phase separation of a protein in a solution is driven by weak, spatially distributed, transient intermolecular interactions. Interestingly, Cdh23 EC1-27 has 440 negatively charged and 222 positively charged amino acid residues distributed throughout its length, thus possessing coacervation propensity. Our *in-silico* search too identified the EC regions in Cdh23 as more prone toward phase separation with a propensity score of 1.3 (Fig. S1). Usually, a propensity score higher than 1 is considered as good LLPS candidate (Ambadipudi et al., 2017). We observed a spontaneous formation of liquid droplets of Cdh23 in the presence of inert crowder molecules like polyethylene glycol (PEG)

above a critical protein concentration of 2.5 μM (Fig. 1 C). The phase-separated state is stable over a range of buffer ionic strength. To visually track the phase separations in real-time under a fluorescence microscope, we recombinantly tagged eGFP at the C-terminal of Cdh23 EC1-27. Fusion among floating droplets, the gold standard for liquid condensates, is also noticed among Cdh23 condensates, indicating the fluid nature of the droplets (Fig. 1 D and Video 1 A). Further from the time-trace analysis of the fusion events, we measured an average fusion-time of 5.0 ± 1.2 s, in range with other proteins that undergo LLPS (Wang et al., 2019) (Fig. S2 and Video 1 B).

Reportedly, Cdh23 mediates both homophilic and heterophilic trans-interactions. Two trans-interactions with two distinct binding affinities are reported between Cdh23 and Pcdh15 (Narui and Sotomayor, 2018). The most robust trans-conformation with a dissociation constant of < 1 μM was notified for the canonical variant. The second *trans*-conformation with a higher dissociation constant of 5 μM was observed for a truncated variant. It was, therefore, necessary to block the interference of the specific trans-interactions and measure the extent of droplet formation. Notably, the heterophilic trans-interaction with Pcdh15 has the highest affinity (Table 1) (Choudhary et al., 2020, Singaraju et al., 2019, Sotomayor et al., 2012). We accordingly blocked the trans-interacting sites of Cdh23 with ligand-protein Pcdh15 EC1-2. As a precaution, we first facilitated the heterophilic trans-interactions with an abundance of Pcdh15 EC1-2 (20 μM) in the experiment buffer and carefully altered the solution's ionic strength from an unfavorable phase separation condition to a favorable state via dialysis (Materials and Methods). We observed LLPS of Cdh23 EC1-27 and Pcdh15 EC1-2 complex, indicating that the droplets are predominantly due to interactions among EC domains other than EC1-2 of Cdh23 (Fig. S5). Notably, the droplets of Cdh23 EC1-27 without Pcdh15 EC1-2 were more extensive than with Pcdh15 EC1-2, indicating that the additional trans-interactions contribute to the phase separation *in vitro* but are not essential for the LLPS. Overall, Cdh23 EC1-27 undergoes LLPS under physiological conditions, and the liquid droplets follow the characteristic feature of protein condensates.

Since the foundation of the dynamic condensed phase in a solution is transient and weak intermolecular interactions, the phase separated droplets rapidly and reversibly undergo mixing in the presence of interaction blockers. 1,6-hexanediol (1,6-HD) is one of such widely used aliphatic alcohol that weakens the hydrophobic interactions critical for LLPS and inhibits the condensation of solutes to liquid droplets (Itoh et al., 2021, Duster et al., 2021). We too noticed complete disruption of liquid droplets of Cdh23 and mixing of the protein in the solution (Fig. S6).

Cdh23 forms lateral clusters on the vesicle membrane without any influence of trans-interactions

Does the weak and nonspecific transient intermolecular interactions enough for lateral clustering of Cdh23 on a membrane? We, thereafter, immobilized the eGFP modified Cdh23 on giant

unilamellar vesicles (GUVs) and allowed free-diffusion (See Methods). Fluorescence recovery after photobleaching (FRAP) has been a valuable tool to quantify the clustering of molecules from the diffusion-rates (Pincet et al., 2016, Kanaan et al., 2020). Accordingly, we performed FRAP experiments on GUVs where the C-terminal of Cdh23-GFP proteins were anchored via affinity (Fig. 2 A and B) (See Methods). We recorded a slow diffusion-rate of 0.24 $\mu m^2/s$ for Cdh23 (Table 2). Treatment of 1,6-HD that blocks the transient interactions, enhances the rate of diffusion of proteins significantly to 0.43 $\mu m^2/s$, confirming that the weak, transient intermolecular interactions are able to form lateral clusters of Cdh23 on a membrane (Fig. 2 C). Moreover, we tracked the fluorescence recovery over a cross-section and noticed the recovery two-dimensionally, indicating the lateral clustering is distributed over the GUV surface without any influence of trans-interactions.

LLPS helps in faster cell-cell aggregation

How does the lateral clustering of Cdh23 contribute to cells? Cadherins generally form anchoring junctions with the neighboring cells. Cdh23 is no different from the other family members and mediates vital cell-cell adhesion junctions in several tissues like the kidney, muscle, testes, and heart (Singaraju et al., 2019, Sannigrahi et al., 2019, Sotomayor et al., 2012, Li et al., 2019). We, therefore, verified the effect of the lateral condensations of Cdh23 in cell-cell adhesion, more importantly, where lateral-clustering precedes the trans-interactions. We hypothesized that lateral clustering of Cdh23 on a membrane would increase the effective intercellular interacting interface and accelerate cell-adhesion kinetics. We thus monitored the aggregation-kinetics of HEK293 cells exogenously expressing Cdh23 and estimated the adhesion-rate constants from the Von Bertalanffy kinetic model fit (West and Newton, 2019, Benzekry et al., 2014) (Materials and Methods). Further, we measured the aggregation kinetics of the same cells but in the presence of 1,6-HD, where clustering of Cdh23 is blocked. As expected, we observed a significantly rapid aggregation-kinetics of HEK293 cells exogenously expressing Cdh23 EC1-27 ($rate\ constant, a_{on}^{0} = 2.1 \times 10^{-3}\ min^{-1}$) than the cells without lateral clustering(Fig. 3 A and B). Importantly, cells in both the experiments formed Cdh23 mediated matured cell-cell junction after incubation, warranting the unaltered functionality of Cdh23 in the presence of 1,6-HD. HEK293 cells treated with siRNA for endogenous Cdh23 showed no aggregation within the experiment time.

Does cis-clustering on cell membrane depend on the extent of surface coverage by Cdh23? To check, we monitored the cell-aggregation kinetics among cancer cell lines, HEK293, HeLa, HaCaT, and A549 that express endogenous Cdh23 differentially. Our results from qRT-PCR and western blot, in corroboration with TCGA, indicate higher endogenous expression of Cdh23 in A549, HaCaT cells and comparatively lower expression in HEK293, HeLa cell-lines (Fig. S7 A). Amongst all in the list, HeLa has the least expression. We performed the cell-aggregation assays in the previously optimized buffer condition and noticed significantly faster cell-aggregations for A549 and HaCat, than the low-expressing cell lines (HEK293 and HeLa). HeLa did not aggregate within the experiment time (Fig. 4 A and B). To conclude the differences in

aggregation kinetics based on the extent of the lateral-clustering, we performed the aggregation kinetics of A549 and HEK293 cells in the presence of 1,6-HD. The aggregation kinetics of both cells dropped significantly in the presence of 1,6-HD (Fig. 5 A and B) and became comparable among each other. Overall, the kinetic data w/o 1,6-HD indicate that the differences in cell-adhesion kinetics of A549 and HEK293 cells without 1,6-HD are due to differences in the extent of lateral-clustering of Cdh23. When chemical treatments abolish the lateral-clustering, the individual Cdh23 molecules on the cell membrane follow the trans-mediated diffusion-trap kinetics for cell adhesion, similar to classical cadherins. While the lateral-clustering increases the effective binding interface on a cell membrane and kinetically facilitates the cell adhesion, the diffusion trap is instead driven by the binding affinities between partners and, thus, independent of the surface coverage.

Fluidic nature of Cdh23 clusters on the cell membrane

To monitor the dynamics of Cdh23 at the cell-cell adhesion junction, we performed FRAP experiments on the intercellular junctions of HEK293 cells that are stably transfected with Cdh23. The protein was recombinantly tagged with eGFP at the C-terminal. We noticed localization of eGFP at the cell-cell junctions as expected for Cdh23 (Fig. 6 A) and photobleached a confocal volume. Next, we monitored the fluorescence recovery along a line across the photobleaching spot (Fig. 6 B and C). This is to identify if the recovery is from the new Cdh23 exported and recruited to the membrane by cells or diffusion of membrane-bound proteins. The fluorescence intensity profile across the line is expected to follow an inverted Gaussian profile with a deep at the center of the photobleaching spot (Fig. 6 D). We noticed widening in the Gaussian profiles with recovery, characteristics of diffusion of active proteins from the surrounding membrane. Recruitment of new proteins, in general, recovers the fluorescence intensity without diluting the surroundings, thus with a little widening of the Gaussian width (Erami et al., 2016). Next, we plotted the width of the Gaussian (σ^2) with time-lapsed after photobleaching and fit to the linear equation and estimated the diffusion-coefficient of Cdh23 clusters at the cell-cell junctions (Fig. 6 E) (Materials and Methods). The diffusion-coefficient of Cdh23 clusters at the cell-cell junctions is $0.6\text{x}10^{-3} \pm 0.1\text{x}10^{-3}$ $\mu m^2\ s^{-1}$, 8-fold slower than the reported diffusion-coefficient of classical E-cadherin ($D_{eff} = 4.8\text{x}10^{-3} \pm 0.3\text{x}10^{-3}$ $\mu m^2\ s^{-1}$) clusters of ~1000 molecules (Erami et al., 2016). Overall, our FRAP data indicates that Cdh23 at the cell-cell junction is fluidic and diffuse in clusters.

Discussion

Specific intermolecular interactions among the EC domains has been driving the linear cis-clustering of classical cadherins. The molecular interactions that expand the spread of cadherin-clusters on a membrane is still not well-understood. It is proposed that the linear cis-interactions are expanded dimensionally via intercellular trans-interactions. However, clustering of cadherins on a membrane without trans-interactions is also reported. It is, therefore, a long standing challenge in cell-cell adhesion to decipher the molecular model of two-dimensional cellular

junctions. We showed that weak, transient, nonspecific, and spatially distributed multivalent interactions that drive molecules to phase separate in a solution, can be responsible for the two-dimensional spread of cadherin clusters on a membrane even prior to any trans-interactions.

Further, the cis-clusters of cadherins are primarily known to strengthen the trans-interactions at the cell-cell junction (Wu et al., 2010). Our experimental observations, however, identify the independent role of lateral clustering on cell-adhesion kinetics. We noticed that Cdh23 could condensate to clusters at the cell membrane independent of trans-mediated anchorage to neighbouring cells, and as super-adhesive, can rapidly seize the floating cells into aggregates. Though the implication of rapid cell-cell adhesion/communication in physiology or life sciences is not yet clear. Cdh23, among other cadherins, is significantly overexpressed in tumor-infiltrating M2-type macrophages (Poczobutt et al., 2016) and microglia (Zhang et al., 2016, Zhang et al., 2014) (Fig. S7 B). M2-type macrophages associate with the circulatory tumor cells (CTCs) on the go and help in metastasis. A quick cell-cell adhesion is thus essential in this process. Though speculative, the fast adhesion between M2 macrophages and CTCs is facilitated by the condensed Cdh23 droplets.

Moreover, Cdh23 may not be the only cadherin in the family that may undergo lateral clustering on membrane without trans-interaction. The Catgranule algorithm estimated the CDF score of more than 1 for many other cadherins (Table 3), considering only the ectodomains. In general, with a CDF of more than 1, the proteins show a tendency for LLPS via nonspecific and transient intermolecular interactions. Accordingly, Fat-cadherin, Dacshous-cadherin, desmosomes, and cadherin-22 have CDF scores of more than 1, and can undergo LLPS. Interestingly, most of these cadherins are associated with special cell-cell junctions. For instance, fat-cadherin and dacshous cadherin-mediated heterophilic junctions exclusively regulate the epithelial cell-size dynamics (ECD) under the mechanical cues during morphogenesis (Kumar et al., 2020), desmoglein-2 forms heterophilic interactions with other isoforms of desmosomal cadherins and form Ca^{2+}-independent hyper-adhesive desmosomal junctions in tissues like skin, heart that are exposed to physical forces.

Conclusion

The distinctive features of nonspecific and transient lateral intermolecular interactions, stretchable and tunable to different sizes and shapes, may be helpful in cell-cell junction, which routinely experiences mechanical assault. Our results non only address the molecular cues that spread the lateral clustering of cadherin-junction in two-dimensions, it also deciphers for the first time the kinetic control of cadherin junctions. Identifying the physiological or pathological phenomena that strongly depend on the rapid cell-cell communication and adhesion may open up another exciting field in cell-adhesion.

Materials and Methods

Cloning of domain deletion mutants of Cdh23

The full-length Cdh23 (NP_075859), consisting of 27 EC domains, a transmembrane domain, and a cytoplasmic domain, was a generous gift from Dr. Raj Ladher, NCBS, Bangalore. Using this construct, we recombinantly generated domain deletion mutants. We have subcloned the same construct in pcDNA3.1 (+) plasmid, which codes for Neomycin resistance. All the constructs were cloned between NheI and XhoI restriction sites with (S)-Sortase-tag (LPETGG)-(G)-eGFP-tag and (H)-His-tag; SGH-tag at downstream (C-terminus of the protein) in the same order. All the recombinant constructs were verified through double digestion, PCR amplification, and DNA sequencing.

Protein expression and purification

All recombinant Cdh23 variants for *in-vitro* studies were expressed in the ExpiCHO suspension cell system (A29129 ThermoFisher Scientific), following the prescribed protocol for transfection in ExpiCHO cells. After seven days, the culture media was collected by pelleting down the cells at 2000 rpm for 15 min at room temperature. The media was then extensively dialyzed against the dialysis buffer for 48 hours and intermittently changed the buffer every 8 hours. The dialyzed media with proteins were purified using affinity chromatography using Ni-NTA columns. The purity of the samples was checked using SDS-PAGE. Finally, the presence of protein was confirmed using western blotting with specific antibodies against GFP, Cadherin-23, and his-tag.

***In vitro* droplet formation assay**

All purified proteins were prepared in buffer containing 20 mM HEPES, pH 7.5, 100 mM NaCl, 4 mM $CaCl_2$. Before each experiment, the proteins were centrifuged at 15000 rpm at 4°C for 10 min to remove possible nonspecific aggregates. Then proteins were adjusted to reach designated concentrations. Each protein mixture (14 μM for each component) was injected into a homemade chamber and imaged using a Leica microscope (Leica DMi8) using a 40X objective lens. The time-lapse images were taken under bright-field and fluorescence filters. All the assayed droplets were thicker than 6 μm in height, so the central layers of optical sections were chosen for quantification. Over 10 or more droplets were measured for each protein to generate the phase diagram of the condensed phase. The images were analyzed by ImageJ, and the quantification was performed by Origin software.

PICUP

About 5 μM of purified Cdh23 was added with a metal complex containing 15 mM sodium phosphate, pH=7.5, 150 mM NaCl, 0.125 mM [$Ru(bpy)_3Cl_2$], and an electron acceptor, 2.5 mM of Ammonium persulfate (APS), followed by the irradiation of visible light for 0.5 sec. With no delay, the reaction mixture was quenched with 7 μl of 4X SDS-gel loading dye and heated at 95 ºC for 5 minutes. Next, SDS-PAGE and silver-staining were performed consecutively to visualize the cross-linked product. Cdh23 EC1-2 (5 μM) was added to block the trans-homodimerization of Cdh23 during PICUP experiments.

GUVs preparation

The mixture of DOPC (850375P, Sigma-Aldrich), DGS NTA Ni (790404C, Sigma-Aldrich), and DSPE-PEG Biotin2000 (Avanti) lipid solutions dissolved in chloroform was used to prepare GUVs. We followed the electroformation method to prepare the GUVs (Bhatia et al., 2017). Briefly, the calculated amounts of lipids mixture (1 mM DOPC: 1 mM DGS NTA Ni) were spread on the plates and allowed the solvent to evaporate under vacuum. GUVs were harvested in a 350 mM sucrose solution. The formation of GUVs was visualized using phase contrast and fluorescence microscopy (Leica, Dmi8), where the GUVs were labeled with Nile red (1 µM), a fluorescent dye (72485, Sigma-Aldrich).

Tethering GUVs to the functionalized surface and the specific attachment of the protein to GUV membranes

Glass base petri dishes were extensively cleaned with piranha and KOH etching before the protein incubations. The glass surfaces were coated with 1 mg/mL of BSA protein (Albumin, biotin-labeled bovine, A8549 Sigma-Aldrich) by incubating for 2 hours, followed by a wash with MilliQ water. Next, the surfaces were incubated with 0.1 mg/ml of Streptavidin stock (S4762, Sigma-Aldrich) for 1 hour and then washed with water. The GUVs were incubated on the modified surface for 4 hours to anchor them to the surface through the non-covalent interactions between biotin-streptavidin. The surface adhered GUVs were incubated with ~ 6 µM of GFP-tagged proteins at 4 ºC for overnight.

FRAP and analysis

FRAP experiments were performed at the polar region of the tethered GUVs using a super-resolution microscope (ZEISS LSM 980 Airyscan 2) at 63X magnification. The experiments were performed in the presence and absence of 1,6 hexanediol in the buffer.

The fluorescence intensity (normalized) at the selected region was measured for three independent experiments and plotted against the time. Recovery half lifetime ($\tau_{1/2}$) was estimated by the global fit of fluorescence intensity profile with recovery time using the following equation,

$$f(t) = A(1 - e^{-\tau t}),$$ where A indicates the mobile fraction of proteins

and $$\tau_{1/2} = \frac{\ln 0.5}{-\tau}$$

The diffusion coefficient for Cdh23 localized on vesicle membranes was calculated using the equation

$$D = \frac{0.88 * w^2}{4\tau_{1/2}}$$, where W is the radius of the region selected to study FRAP.

LLPS disruption studies

To disrupt the liquid-like clusters, the cells were incubated with 2% (w/v) of 1,6-Hexanediol (H11807, Sigma-Aldrich) for 1 hour. Similarly, 10% (w/v) of 1,6-Hexanediol was used to disrupt the liquid droplets of Cdh23 EC1-27 *in-vitro*.

Western blot and qRT-PCR

The adherent cancer cell lines HeLa, HEK293, A549, and HaCat were obtained from NCCS, Pune. All cells were cultured in high glucose DMEM media (D1152, Sigma-Aldrich) containing 10% FBS and 5% CO_2. We followed the standard protocol(Hirano, 2012) for the western blotting of the lysates from the mentioned cell lines. Cadherin-23 (HPA017232, Sigma-Aldrich and PA5-43398, Invitrogen), eGFP (A11122, Invitrogen), and His-tag (11965085001, Roche) antibodies were used to detect the proteins.

RNA from different cancer cell lines was extracted using RNA isolation kit (Bio Rad) and treated with DNAse using DNAse 1 kit (AMPD1, Sigma-Aldrich). cDNA synthesis was done using a cDNA synthesis kit (Bio Rad). qRT-PCR was performed with the primers probing Cdh23 using the real-time PCR system (CFX96 Bio Rad).

Cell-aggregation assay

After 30 hours of post-transfection, the cells were washed gently with PBS and then resuspended in Hank's buffer supplemented with 10mM Ca^{2+} ions to a final cell count of 10^5 cells. Hank's buffer behaves like an incomplete media maintaining the osmolarity of the solution with the cells avoiding any bursting or shrinking of cells throughout the entire duration of the assay. After resuspending, the cells were imaged with a bright-field filter at 10X magnification using a Leica Inverted Microscope (Leica DMi8) over a time trace for 2 hours. The images were collected at 10 min, 15min, 30 min, 45 min, 60 min, and 120 min when all the cells aggregated completely. The image analysis for measuring the area of each aggregate was done in ImageJ software. The aggregates with at least 5 cells are considered for the analysis. The mean area of aggregates over four different focal positions was measured and plotted against time. The aggregate size was compared over varying domain lengths for Cdh23. We performed all cell aggregation experiments at fixed cell-types and numbers. 1% (w/v) of 1,6-Hexanediol was added in Hank's buffer for disrupting the LLPS during the cell-aggregation assays.

Fitting the cell aggregation data to a model

We have used the Von Bertalanffy model (West and Newton, 2019, Benzekry et al., 2014) to quantify the rate of cell-cell aggregation for HEK293 cells transfected with Cdh23 EC1-27. The net rate of cell aggregation is proportional to the total area of aggregate. In the absence of any dissociation in our experiment timescale, we have neglected the loss term in the equation (a special case of the Von Bertalanffy model). Finally, we fit the cell aggregation data for an experimental condition over time using the following rate-equation:

$$\frac{dA}{dt} = a_{on}^{0}.A^{\gamma}$$

The model is solved and written explicitly as, $A(t) = \left(a_{on}^{0}.t.(1-\gamma)\right)^{\frac{1}{1-\gamma}}$, where, a_{on}^{0} represents the rate-constant, A represents the area of aggregate, $t$is the independent variable (time), and γ represents the growth of aggregate. $a_{on}^{0}$is an inherent property and γ is dependent on the cell types and their heterogeneity. While fitting, we, therefore, performed global fits and shared the value of γ (Table S1).

Live cell imaging and FRAP analysis

Stably expressing Cdh23 HEK293 cells grown for confluency on a 35mm glass-base petri dish were used for imaging. A super-resolution microscope (Zeiss LSM980 Airyscan 2) was used to image the cells maintained at 37 ºC and 5% CO2. FRAP was performed on a confocal volume of 1 µm diameter at the cell-cell junctions where localization of eGFP was noticed. ImageJ software was used to measure the fluorescence intensity profiles of the line segment of 4 µm drawn across the photobleached region (line-scan analysis). The fluorescence intensity profiles (normalized) at different time points were fit to the Gaussian function in origin software. The fitted widths obtained at different time points were plotted against recovery time, and fit to linear regression to estimate the diffusion coefficient from the slope (Erami et al., 2016).

Acknowledgments

This work was supported by the DBT/Wellcome Trust India Alliance Fellowship [grant number: IA/I/15/1/501817] awarded to SR.

SR acknowledges and thanks Dr. Raj K. Ladher, NCBS, for generously donating the Cadherin-23 plasmid. SR acknowledges the financial support by the DBT/Wellcome Trust India Alliance, Indian Institute of Science Education and Research Mohali (IISERM), and Centre for Protein Science Design and Engineering (CPSDE), Indian Institute of Science Education and Research Mohali. GSS, CSS, and AS sincerely thank IISERM for financial support. SD thanks DBT/Wellcome Trust India Alliance for Project Assistant Fellowship awarded to SR AK is grateful to DST Inspire for funding.

We thank Mr. Taseen Ahmad for assisting in acquiring super-resolution microscopy data.

The authors declare no competing financial interests.

Author Contributions

SR has supervised the project. GSS, SD, AS, and AK did the cloning, expression, and purification. GSS and CSS recorded and analyzed droplet condensation and cell-aggregation experiments. CSS carried out the curve fitting. VK performed PICUP experiments. CSS did the

live-cell imaging and FRAP experiments. VK, SKG and CSS performed GUV experiments.GSS, VK and CSS made the figures. SR and CSS wrote the manuscript. GSS, CSS and SR edited the manuscript. CSS and GSS have contributed equally.

References

ALTIN, J. G. & PAGLER, E. B. 1995. A one-step procedure for biotinylation and chemical cross-linking of lymphocyte surface and intracellular membrane-associated molecules. *Anal Biochem,* 224, 382-9.

AMBADIPUDI, S., BIERNAT, J., RIEDEL, D., MANDELKOW, E. & ZWECKSTETTER, M. 2017. Liquid–liquid phase separation of the microtubule-binding repeats of the Alzheimer-related protein Tau. *Nature Communications,* 8, 275.

BANJADE, S. & ROSEN, M. K. 2014. Phase transitions of multivalent proteins can promote clustering of membrane receptors. *Elife,* 3.

BENZEKRY, S., LAMONT, C., BEHESHTI, A., TRACZ, A., EBOS, J. M., HLATKY, L. & HAHNFELDT, P. 2014. Classical mathematical models for description and prediction of experimental tumor growth. *PLoS Comput Biol,* 10, e1003800.

BEUTEL, O., MARASPINI, R., POMBO-GARCIA, K., MARTIN-LEMAITRE, C. & HONIGMANN, A. 2019. Phase Separation of Zonula Occludens Proteins Drives Formation of Tight Junctions. *Cell,* 179, 923-936 e11.

BHATIA, T., CORNELIUS, F. & IPSEN, J. H. 2017. Capturing suboptical dynamic structures in lipid bilayer patches formed from free-standing giant unilamellar vesicles. *Nat Protoc,* 12, 1563-1575.

BUCHAN, J. R. & PARKER, R. 2009. Eukaryotic stress granules: the ins and outs of translation. *Mol Cell,* 36, 932-41.

CHOUDHARY, D., NARUI, Y., NEEL, B. L., WIMALASENA, L. N., KLANSECK, C. F., DE-LA-TORRE, P., CHEN, C., ARAYA-SECCHI, R., TAMILSELVAN, E. & SOTOMAYOR, M. 2020. Structural determinants of protocadherin-15 mechanics and function in hearing and balance perception. *Proc Natl Acad Sci U S A,* 117, 24837-24848.

DUSTER, R., KALTHEUNER, I. H., SCHMITZ, M. & GEYER, M. 2021. 1,6-Hexanediol, commonly used to dissolve liquid-liquid phase separated condensates, directly impairs kinase and phosphatase activities. *J Biol Chem,* 296, 100260.

ELBAUM-GARFINKLE, S. 2019. Matter over mind: Liquid phase separation and neurodegeneration. *J Biol Chem,* 294, 7160-7168.

ERAMI, Z., HERRMANN, D., WARREN, S. C., NOBIS, M., MCGHEE, E. J., LUCAS, M. C., LEUNG, W., REISCHMANN, N., MROWINSKA, A., SCHWARZ, J. P., KADIR, S., CONWAY, J. R. W., VENNIN, C., KARIM, S. A., CAMPBELL, A. D., GALLEGO-ORTEGA, D., MAGENAU, A., MURPHY, K. J., RIDGWAY, R. A., LAW, A. M., WALTERS, S. N., GREY, S. T., CROUCHER, D. R., ZHANG, L., HERZOG, H., HARDEMAN, E. C., GUNNING, P. W., ORMANDY, C. J., EVANS, T. R. J., STRATHDEE, D., SANSOM, O. J., MORTON, J. P., ANDERSON, K. I. & TIMPSON, P. 2016. Intravital FRAP Imaging using an E-cadherin-GFP Mouse Reveals Disease- and Drug-Dependent Dynamic Regulation of Cell-Cell Junctions in Live Tissue. *Cell Rep,* 14, 152-167.

FANCY, D. A. & KODADEK, T. 1999. Chemistry for the analysis of protein-protein interactions: rapid and efficient cross-linking triggered by long wavelength light. *Proc Natl Acad Sci U S A,* 96, 6020-4.

GALL, J. G. 2003. The centennial of the Cajal body. *Nat Rev Mol Cell Biol,* 4, 975-80.

HARRISON, O. J., JIN, X., HONG, S., BAHNA, F., AHLSEN, G., BRASCH, J., WU, Y., VENDOME, J., FELSOVALYI, K., HAMPTON, C. M., TROYANOVSKY, R. B., BEN-SHAUL, A., FRANK, J., TROYANOVSKY, S. M., SHAPIRO, L. & HONIG, B. 2011. The extracellular architecture of adherens junctions revealed by crystal structures of type I cadherins. *Structure,* 19, 244-56.

HIRANO, S. 2012. Western blot analysis. *Methods Mol Biol,* 926, 87-97.

ITOH, Y., IIDA, S., TAMURA, S., NAGASHIMA, R., SHIRAKI, K., GOTO, T., HIBINO, K., IDE, S. & MAESHIMA, K. 2021. 1,6-hexanediol rapidly immobilizes and condenses chromatin in living human cells. *Life Sci Alliance,* 4.

KANAAN, N. M., HAMEL, C., GRABINSKI, T. & COMBS, B. 2020. Liquid-liquid phase separation induces pathogenic tau conformations in vitro. *Nat Commun,* 11, 2809.

KLUS, P., BOLOGNESI, B., AGOSTINI, F., MARCHESE, D., ZANZONI, A. & TARTAGLIA, G. G. 2014. The cleverSuite approach for protein characterization: predictions of structural properties, solubility, chaperone requirements and RNA-binding abilities. *Bioinformatics,* 30, 1601-8.

KUMAR, A., RIZVI, M. S., ATHILINGAM, T., PARIHAR, S. S. & SINHA, P. 2020. Heterophilic cell-cell adhesion of atypical cadherins Fat and Dachsous regulate epithelial cell size dynamics during Drosophila thorax morphogenesis. *Mol Biol Cell,* 31, 546-560.

LATONEN, L. 2019. Phase-to-Phase With Nucleoli - Stress Responses, Protein Aggregation and Novel Roles of RNA. *Front Cell Neurosci,* 13, 151.

LI, Q., CHENG, Z., ZHOU, L., DARMANIS, S., NEFF, N. F., OKAMOTO, J., GULATI, G., BENNETT, M. L., SUN, L. O., CLARKE, L. E., MARSCHALLINGER, J., YU, G., QUAKE, S. R., WYSS-CORAY, T. & BARRES, B. A. 2019. Developmental Heterogeneity of Microglia and Brain Myeloid Cells Revealed by Deep Single-Cell RNA Sequencing. *Neuron,* 101, 207-223 e10.

MAHEN, R. & VENKITARAMAN, A. R. 2012. Pattern formation in centrosome assembly. *Curr Opin Cell Biol,* 24, 14-23.

MITCHELL, S. F., JAIN, S., SHE, M. & PARKER, R. 2013. Global analysis of yeast mRNPs. *Nat Struct Mol Biol,* 20, 127-33.

NARUI, Y. & SOTOMAYOR, M. 2018. Tuning Inner-Ear Tip-Link Affinity Through Alternatively Spliced Variants of Protocadherin-15. *Biochemistry,* 57, 1702-1710.

PATEL, A., MALINOVSKA, L., SAHA, S., WANG, J., ALBERTI, S., KRISHNAN, Y. & HYMAN, A. A. 2017. ATP as a biological hydrotrope. *Science,* 356, 753-756.

PINCET, F., ADRIEN, V., YANG, R., DELACOTTE, J., ROTHMAN, J. E., URBACH, W. & TARESTE, D. 2016. FRAP to Characterize Molecular Diffusion and Interaction in Various Membrane Environments. *PLoS One,* 11, e0158457.

POCZOBUTT, J. M., DE, S., YADAV, V. K., NGUYEN, T. T., LI, H., SIPPEL, T. R., WEISER-EVANS, M. C. & NEMENOFF, R. A. 2016. Expression Profiling of Macrophages Reveals Multiple Populations with Distinct Biological Roles in an Immunocompetent Orthotopic Model of Lung Cancer. *J Immunol,* 196, 2847-59.

SANNIGRAHI, M. K., SRINIVAS, C. S., DEOKATE, N. & RAKSHIT, S. 2019. The strong propensity of Cadherin-23 for aggregation inhibits cell migration. *Mol Oncol,* 13, 1092-1109.

SINGARAJU, G. S., SAGAR, A., KUMAR, A., SAMUEL, J. S., HAZRA, J. P., SANNIGRAHI, M. K., YENNAMALLI, R. M., ASHISH, F. & RAKSHIT, S. 2019. Structural basis of the strong cell-cell junction formed by cadherin-23. *FEBS J.*

SOTOMAYOR, M., WEIHOFEN, W. A., GAUDET, R. & COREY, D. P. 2010. Structural determinants of cadherin-23 function in hearing and deafness. *Neuron,* 66, 85-100.

SOTOMAYOR, M., WEIHOFEN, W. A., GAUDET, R. & COREY, D. P. 2012. Structure of a force-conveying cadherin bond essential for inner-ear mechanotransduction. *Nature,* 492, 128-32.

WANG, Z., ZHANG, G. & ZHANG, H. 2019. Protocol for analyzing protein liquid–liquid phase separation. *Biophysics Reports,* 5, 1-9.

WEST, J. & NEWTON, P. K. 2019. Cellular interactions constrain tumor growth. *Proc Natl Acad Sci U S A,* 116, 1918-1923.

WU, Y., JIN, X., HARRISON, O., SHAPIRO, L., HONIG, B. H. & BEN-SHAUL, A. 2010. Cooperativity between trans and cis interactions in cadherin-mediated junction formation. *Proc Natl Acad Sci U S A,* 107, 17592-7.

WU, Y., KANCHANAWONG, P. & ZAIDEL-BAR, R. 2015. Actin-delimited adhesion-independent clustering of E-cadherin forms the nanoscale building blocks of adherens junctions. *Dev Cell,* 32, 139-54.

ZHANG, Y., CHEN, K., SLOAN, S. A., BENNETT, M. L., SCHOLZE, A. R., O'KEEFFE, S., PHATNANI, H. P., GUARNIERI, P., CANEDA, C., RUDERISCH, N., DENG, S., LIDDELOW, S. A., ZHANG, C., DANEMAN, R., MANIATIS, T., BARRES, B. A. & WU, J. Q. 2014. An RNA-sequencing transcriptome and splicing database of glia, neurons, and vascular cells of the cerebral cortex. *J Neurosci,* 34, 11929-47.

ZHANG, Y., SLOAN, S. A., CLARKE, L. E., CANEDA, C., PLAZA, C. A., BLUMENTHAL, P. D., VOGEL, H., STEINBERG, G. K., EDWARDS, M. S., LI, G., DUNCAN, J. A., 3RD, CHESHIER, S. H., SHUER, L. M., CHANG, E. F., GRANT, G. A., GEPHART, M. G. & BARRES, B. A. 2016. Purification and Characterization of Progenitor and Mature Human Astrocytes Reveals Transcriptional and Functional Differences with Mouse. *Neuron,* 89, 37-53.

Abbreviations

AUC Analytical UltraCentrifugation

Cdh23 Cadherin-23

CDF Cumulative Distribution Function

CD Cytosolic domain

EC Extracellular

EC1-27 Extracellular 1-27 domains

eGFP Enhanced Green fluorescent protein

FRAP Fluorescence Recovery After Photobleaching

GUV Giant unilamellar vesicles

1,6-HD 1,6-Hexanediol

ITC Isothermal titration calorimetry

LLPS Liquid- Liquid Phase Separation

Pcdh15 Protocadherin-15

PICUP Photoinduced cross-linking of unmodified proteins

qRT-PCR Quantitative Real-time polymerase chain reaction

SPR Surface Plamon Resonance

TM Transmembrane

Figures and Tables

Figure 1

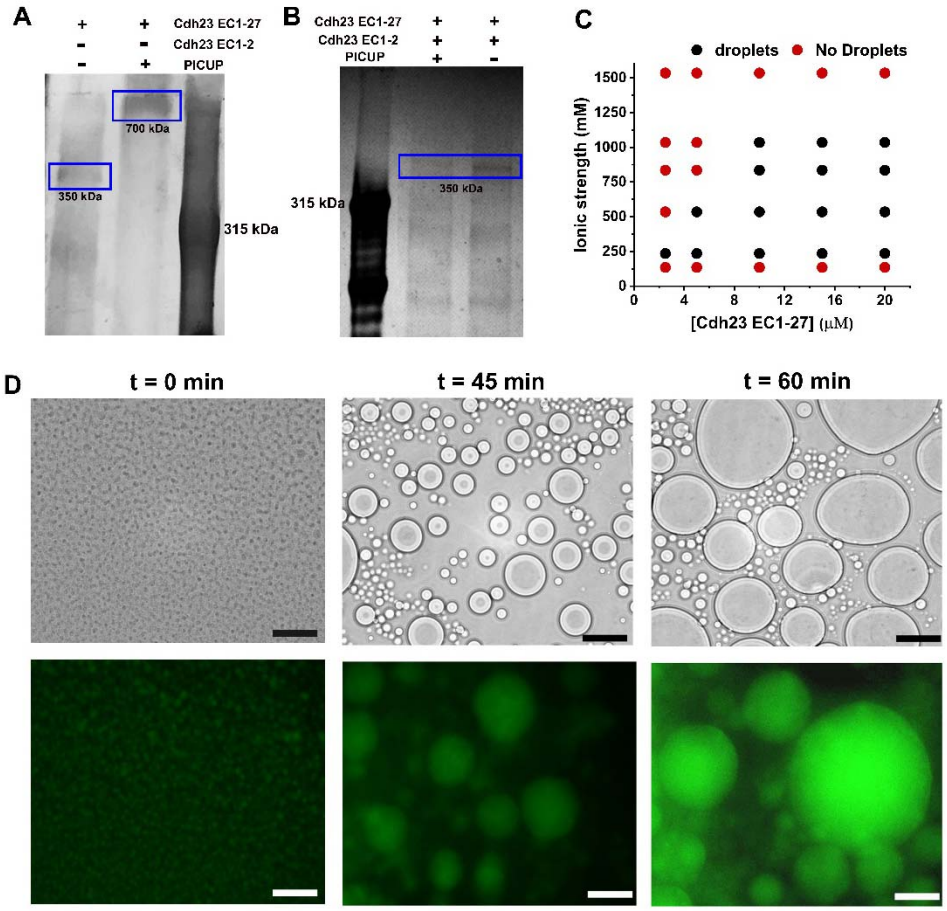

Figure 1. The weak, nonspecific, and transient interactions among EC domains facilitate the clustering of Cdh23 in the solution. (A) The silver staining of SDS PAGE gel shows the dimer (~700 kDa) of Cdh23 EC1-27 when subjected to PICUP. However, only monomer (~350 kDa) is detected in the absence of PICUP. **(B)** The silver staining of SDS PAGE gel detects only a monomer of Cdh23 on blocking the trans interactions of Cdh23 EC1-27. The trans homophilic interactions of Cdh23 EC1-27 are blocked by incubating with Cdh23 EC1-2. **(C)** Phase diagram of liquid droplets of Cdh23 EC1-27 relating protein concentration and ionic strength of the buffer with droplet formation. **(D)** Representative bright-field images (upper panel), and fluorescence images (lower panel) of liquid droplet-like condensates of Cdh23 EC1-27 at three different time intervals (i) 0 min, (ii) 45 min, and (iii) 60 min. Buffer composition is 20 mM HEPES, 500 mM NaCl and 6 mM $CaCl_2$. Scale bar: 50 µm.

Figure 2

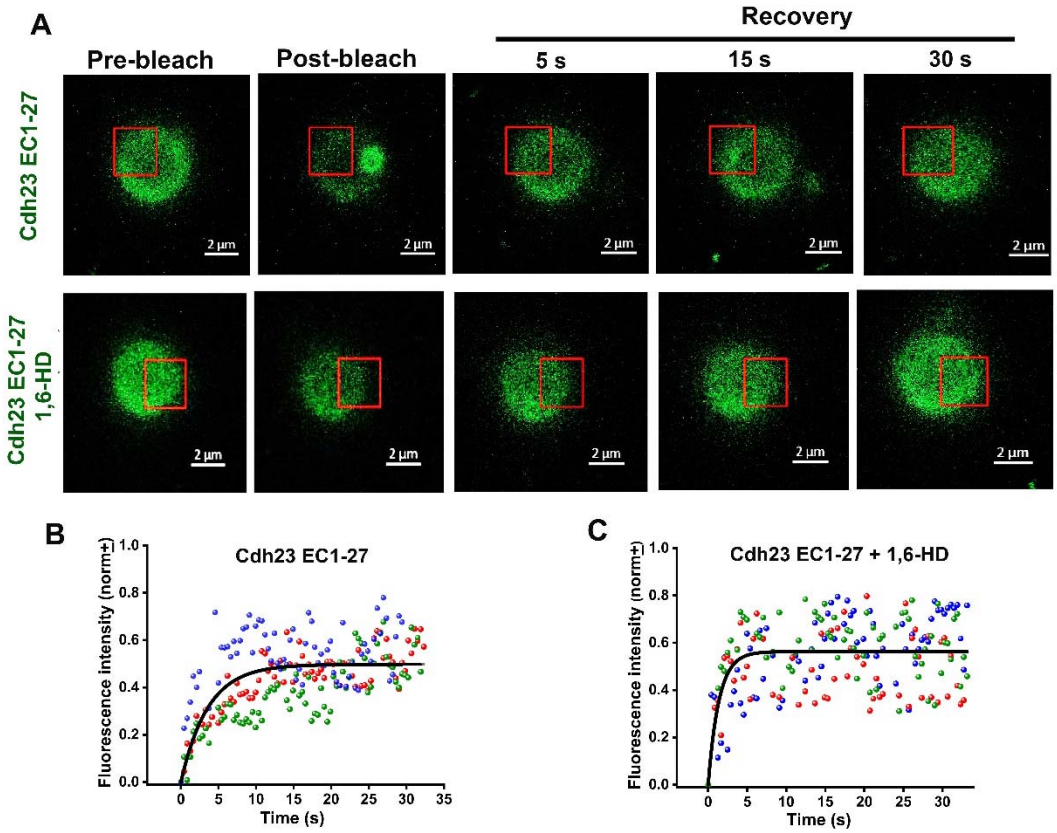

Figure 2. Cdh23 forms lateral clusters on GUV membranes. (A) The fluorescence images indicate the pre-bleach, bleach, and post-bleach recovery regions at the selected time points on GUVs incubated with Cdh23 EC1-27 (upper panel) and 1,6-HD treated Cdh23 EC1-27 (lower panel). The rectangles (red) indicate the polar region of GUV selected for the FRAP study. Scale bar: 2 µm. The fluorescence intensity profile (normalized) at the rectangle (red) region was plotted against recovery time for the Cdh23 EC1-27 (**B**), and 1,6-HD treated Cdh23 EC1-27 (**C**). The solid lines represent the fitting of the fluorescence recovery over time to the model (see methods).

Figure 3

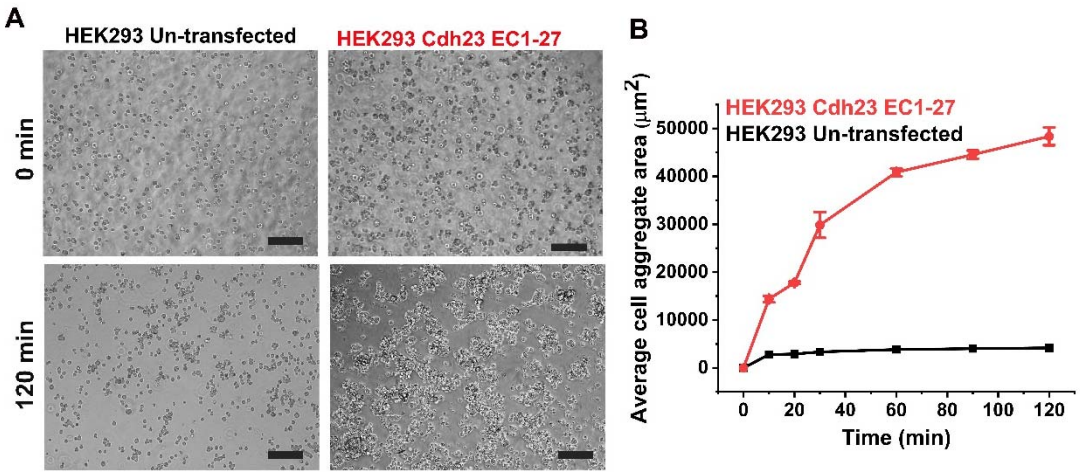

Figure 3. Lateral clustering of Cdh23 on membrane enhances the kinetics of cell-cell adhesion. **(A)** Time-stamp bright-field images of cell-cell aggregations of HEK293 cells untransfected (1st column), and Cdh23 EC1-27 (2nd column). Scale bar: 50 µm. **(B)** The time-dependent growth of the cell-cell aggregation area of HEK293 cells exogenously expressing Cdh23 EC1-27 (red), and untransfected cells (black). The error bars represent the standard error of the mean (SEM) with N=15 aggregates.

Figure 4

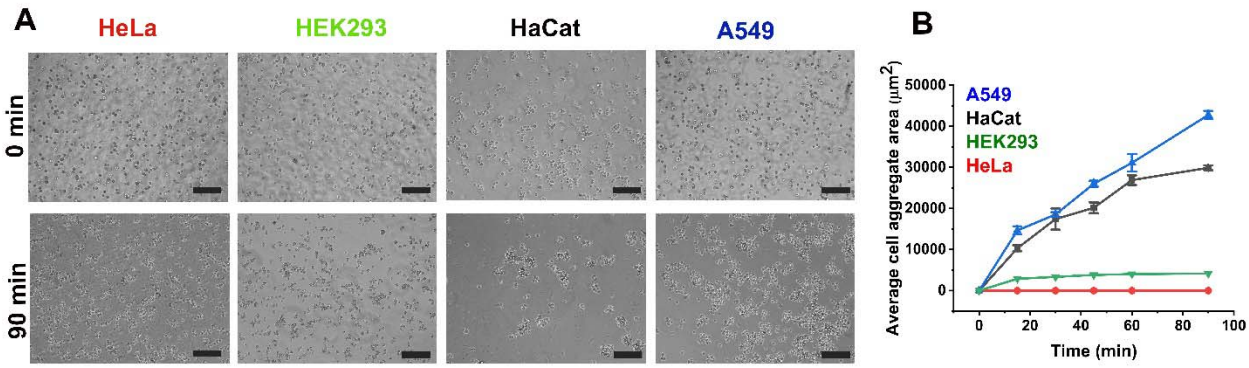

Figure 4. Dependence of cell-cell adhesion rate on the intrinsic expression of Cdh23. (A) Time-stamp bright-field images of cell-aggregates of HeLa, HEK293, HaCat, and A549 cells differentially expressing endogenous Cdh23. Scale bar: 50 µm. (**B)** Growth of cell-cell aggregation area (in μm^2) with time for HeLa (red), HEK293 (green), HaCat. (black) and A549 (blue) cell lines. Error bars represent the standard error of the mean (SEM) for N=15 aggregates.

Figure 5

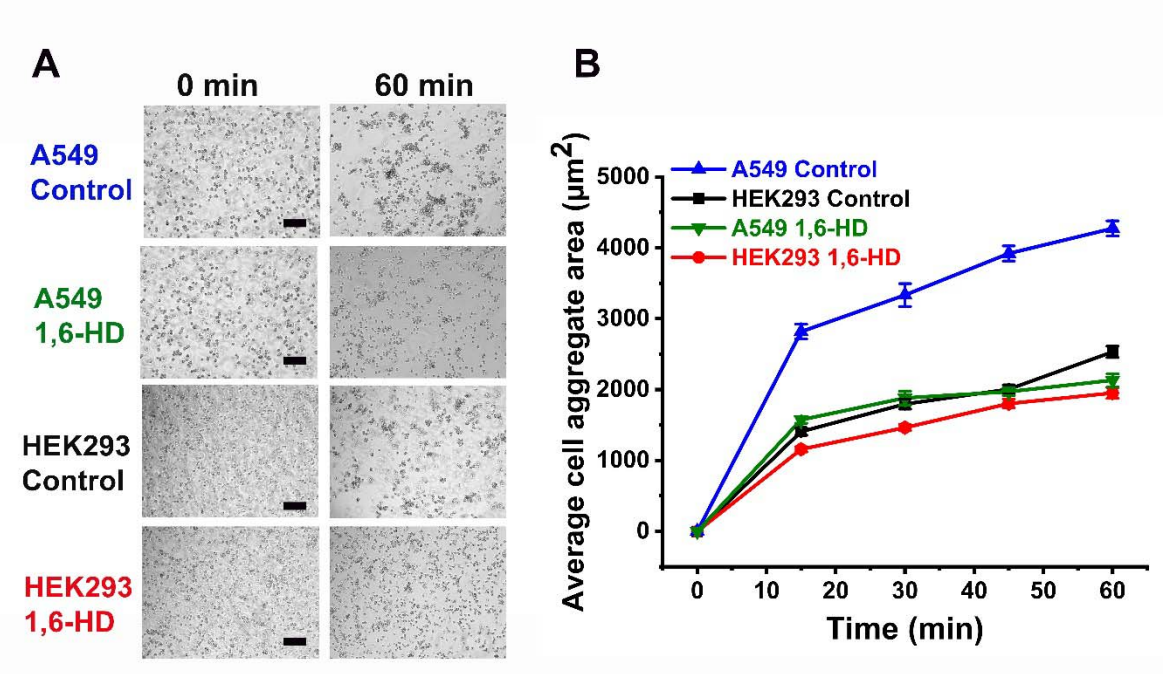

Figure 5. Effect of disrupted cis-clusters on cell-adhesion kinetics. (A) Time-stamp bright-field images of cell aggregates of A549 and HEK293 cells in the absence (control) and presence of 1,6-HD. Scale bar: 50 µm. **(B)** Growth of cell-cell aggregation area (in μm^2) with time for A549 cells in control (blue) and treated with 1,6-HD (Olive), and HEK2923 cells in control (black) and treated with 1,6-HD (red). Error bars represent the standard error of the mean (SEM) for N=15 aggregates.

Figure 6

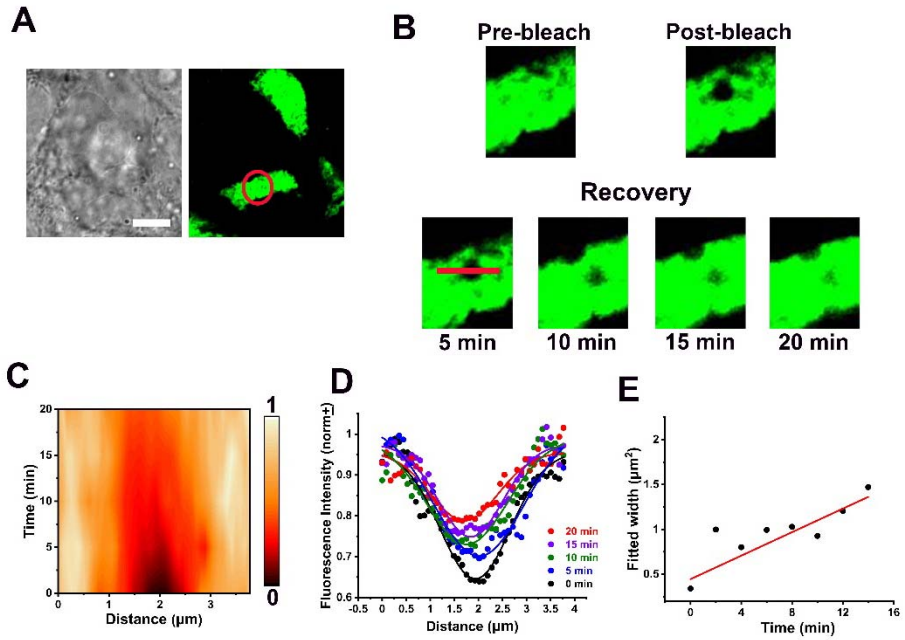

Figure 6. FRAP to probe the fluidic cis-clusters of Cdh23 at the cell-cell junctions. (A) Representative bright field and fluorescence images show the localization of Cdh23 at the cell-cell junction of HEK293 cells exogenously expressing Cdh23. Cdh23 is recombinantly tagged with eGFP at C-terminus. The circle (red) indicates the confocal volume for the FRAP experiment. Scale bar: 10 µm. **(B)** The cross-sections of fluorescence images indicate the regions of pre-bleach, bleach, and post-bleach recovery at the selected time points. The fluorescence recovery is monitored with time along the red line. The length of the line is 4 µm. **(C)** The contour plot represents the spatiotemporal distribution of Cdh23-eGFP along the red line. **(D)** The fluorescence intensity profile along the red line is plotted with the recovery time points. The solid lines are the Gaussian fits. **(E)** The widths (σ^2) from the Gaussian fits are plotted with recovery time. The solid red line is the linear fit to the data to estimate the diffusion-coefficient. Error bars indicate the standard deviation obtained from the Gaussian fit.

Table 1. Binding-affinities of the heterophilic and homophilic trans-complexes of Cdh23 as reported.

Homo/Heterophilic dimer	Interaction geometry	Method	T(ºC)	K_D (μM)	Reference
Cdh23 (EC1-2)-Pcdh15 (EC1-2)	Trans	ITC	10	2.9 ± 0.4	Nature, 2012
Cdh23 (EC1-2)-Pcdh15 (EC1-2)	Trans	SPR	25	0.84 ± 0.03	Biochemistry,2018
Cdh23 (EC1-2)-Cdh23 (EC1-2)	Trans	AUC	20	18 ± 4	FEBS, J.,2019

K_D denotes the dissociation constant

Table 2. Diffusion coefficients for Cdh23 EC1-27 in the presence and absence of 1,6-HD on GUV membranes

	Diffusion coefficient ($\mu m^2/s$)
Cdh23 EC1-27	0.24
Cdh23 EC1-27 + 1,6-HD	0.43

Table 3. CDF scores for different cadherins (EC-domains only) estimated using catGRANULE algorithm.

Cadherins	CDF score
Cdh23	1.259
Pcdh1	1.002
Dcsh1	1.350
FAT1	1.432
FAT2	1.326
FAT3	1.538
FAT4	1.642

CDF score represents the propensity for LLPS

Supplementary information for

Transient interactions drive the lateral clustering of Cadherin-23 on membrane

Cheerneni S Srinivas[1#], Gayathri S Singaraju[1#], Veerpal Kaur[1], Sayan Das[1], Sanat K. Ghosh[2], Amin Sagar[1], Anuj Kumar[2,3], Tripta Bhatia[2*], and Sabyasachi Rakshit[1,3*]

[*]Correspondence to Sabyasachi Rakshit: srakshit@iisermohali.ac.in

[#] Equal contributions

This file includes:

Figures S1 to S7

Legends for videos 1 A and B

Table S1

Supplementary Figures:

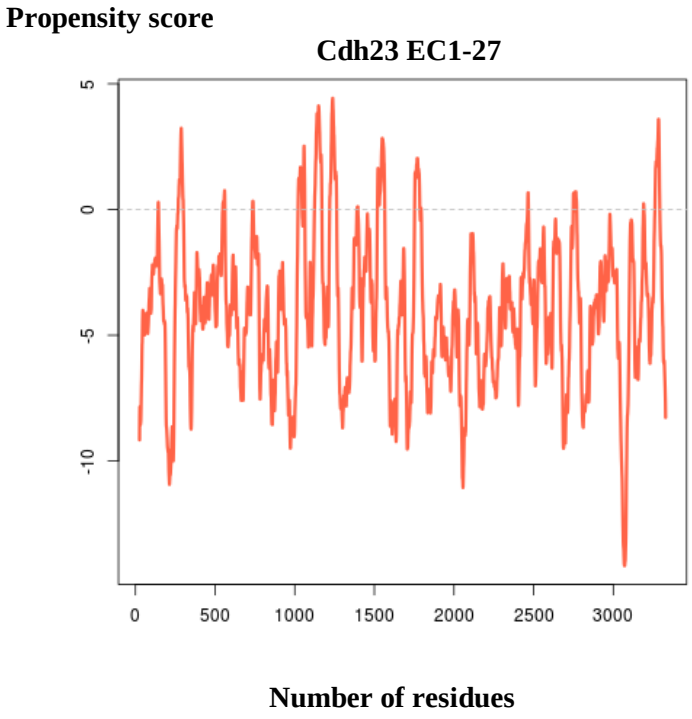

Figure S1. The high propensity of Cdh23 EC1-27 to undergo liquid-liquid phase separation. The plot of the propensity scores estimated using the catGRANULE algorithm for Cdh23 EC1-27 versus the number of residues shows that a higher number of EC domains has a higher probability of undergoing LLPS. The propensity score for Cdh23 EC1-27 is 1.2932.

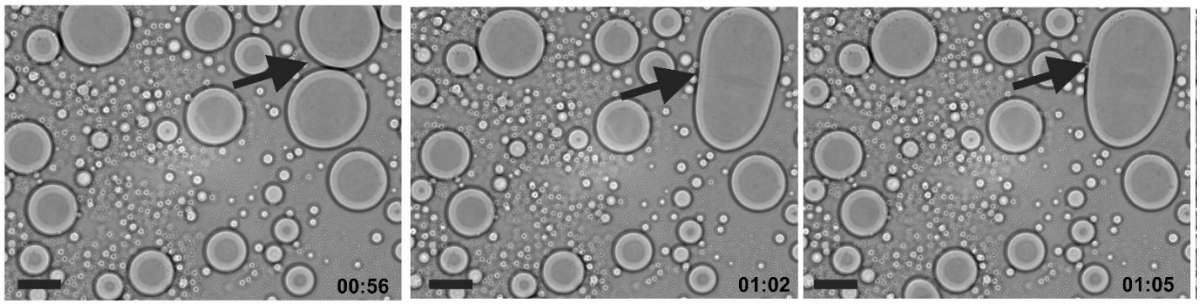

Figure S2. Time-lapse images of droplet fusion (Supporting to Fig. 1 D). The bright-field images with time capture one of the fusion events of liquid droplets of Cdh23 EC1-27. Arrows in black are highlighting the droplets undergoing fusion. Scale bar: 50 µm.

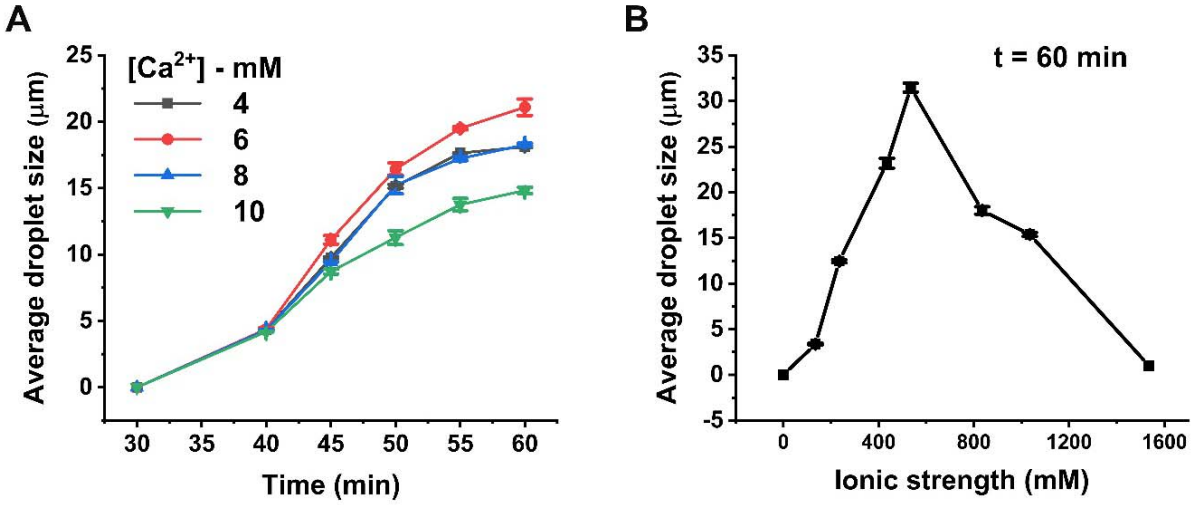

Figure S3. Systematic alterations of Ca^{2+} ions for the optimization of LLPS of Cdh23 EC1-27 (Supporting to Fig. 1 D). (A) The growth of liquid droplets (µm) of Cdh23 EC1-27 with time depends on Ca^{2+} concentration. Error bars represent the standard error of the mean (SEM) for N=30 droplets. (**B)** The liquid droplet size of Cdh23 EC1-27 measured after 60 min of nucleation follows a typical bell-shaped curve with increasing ionic strength of the buffer. Error bars represent SEM with N=30 droplets.

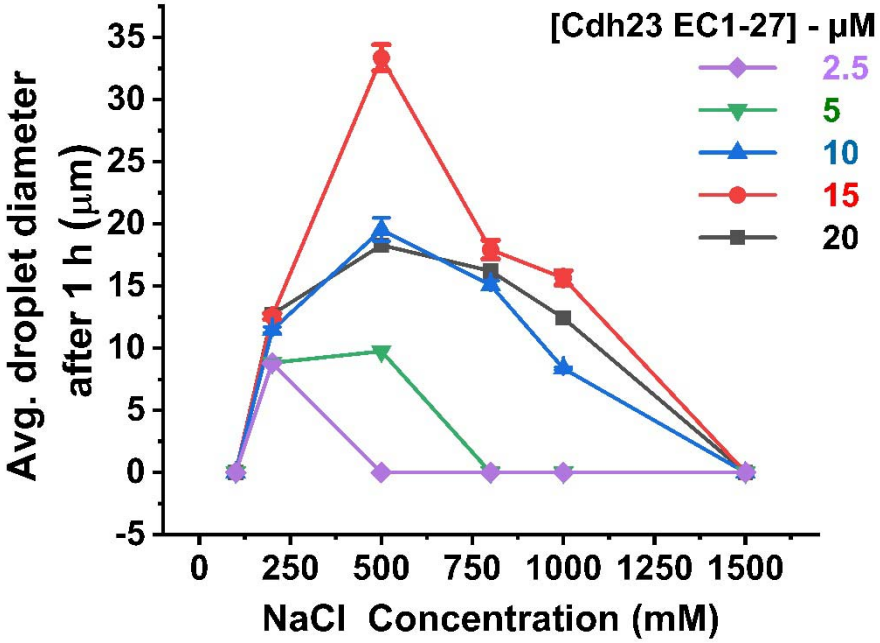

Figure S4. Optimization of LLPS of Cdh23 EC1-27 at varying NaCl and protein concentrations (Supporting to Fig. 1 C). Error bars represent SEM with N=30 droplets.

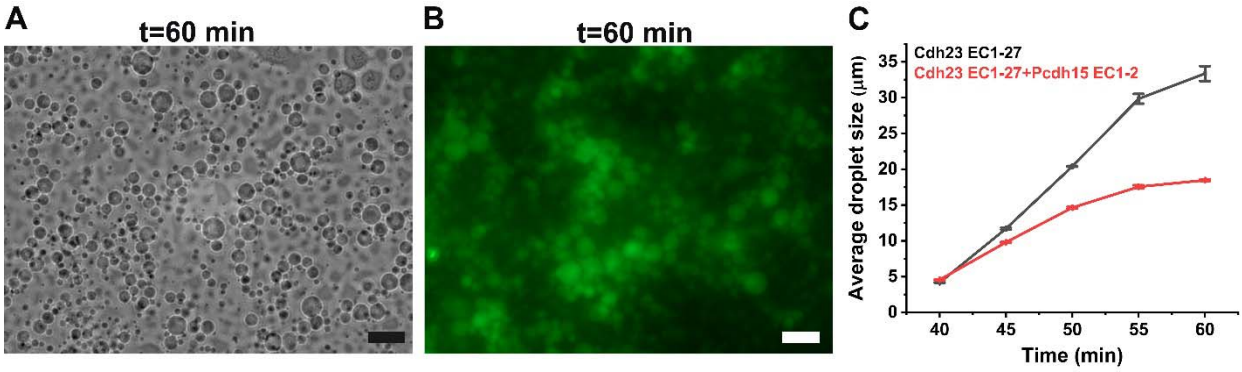

Figure S5. LLPS of Cdh23 EC1-27 in the absence of trans-interactions. (A) Bright-field and **(B)** fluorescence images of liquid droplets of Cdh23 EC1-27 induced by exclusive cis-interactions. The trans-interactions were turned off by introducing Pcdh15 EC1-2 in the buffer. The scale bar is 50 µm. **(C)** The comparative growth kinetics of liquid droplets (µm) of Cdh23 EC1-27 in the absence (black) and presence (red) of Pcdh15 EC1-2. Pcdh15 blocks the homophilic trans-binding interface of Cdh23.

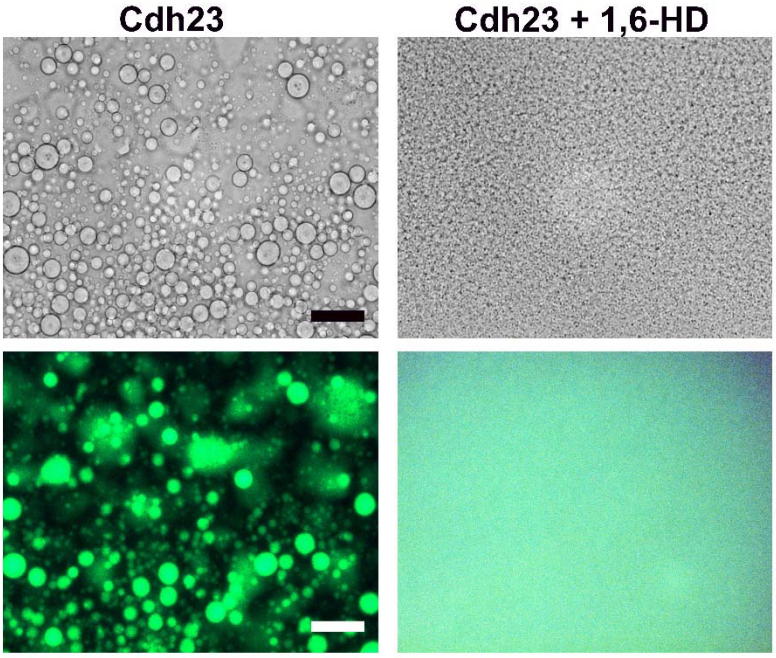

Figure S6. Cis-clustering of Cdh23 drives the LLPS of Cdh23. (A) The representative bright-field and fluorescence images of liquid droplets of Cdh23 EC1-27 in the absence (column 1) and presence (column 2) of 1,6-HD. 1,6-HD disrupted the liquid droplets of Cdh23 EC1-27. Scale bar: 50 µm.

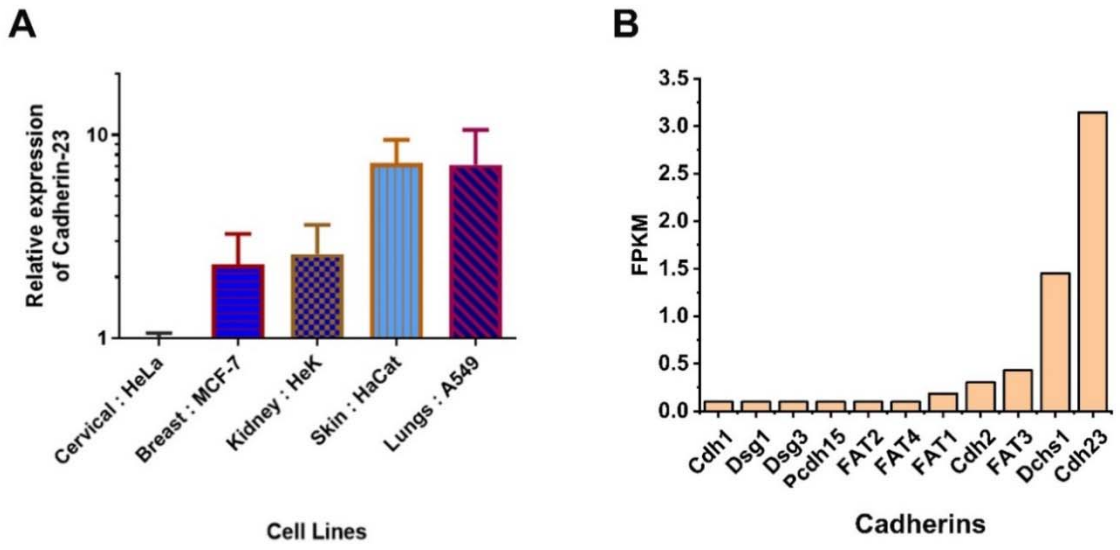

Figure S7. Differential expression of Cdh23 in cancer cell lines and microglia (Supporting to Fig. 4). (**A)** The relative expression of Cdh23 mRNA in different cancer cell lines, namely HeLa, MCF-7, HEK293, HaCat, and A549, was quantified using qRT-PCR. The highest expression is noticed in A549 and the most negligible expression in HeLa. (**B)** The bar plot displays the mRNA expression of different cadherin proteins in microglia cells. FPKM is Fragments Per Kilobase Million essentially represents normalized expression values.

Video 1 A. Fusion of droplets of Cdh23 EC1-27 (Supporting to Fig. 1 F). The fusion of liquid droplets of Cdh23 EC1-27 was captured under a fluorescence (GFP) microscope.

Video 1 B. Fusion of droplets of Cdh23 EC1-27 (Supporting to Fig. 1 E). The fusion of liquid droplets of Cdh23 EC1-27 was captured under a bright field.

Table S1. The value of γ was obtained from fitting the cell aggregation kinetics to the Von Bertalanffy model.

Cell aggregation experiment	**γ**
Cdh23 EC1-27	-2.25
Cdh23 EC1-27 at different Ca^{2+} concentrations	

γ represents the growth of the aggregate.